

# Giant Stark splitting of an exciton in bilayer MoS<sub>2</sub>

Nadine Leisgang<sup>1\*</sup>, Shivangi Shree<sup>2\*</sup>, Ioannis Paradisanos<sup>2\*</sup>, Lukas Sponfeldner<sup>1\*</sup>, Cedric Robert<sup>2</sup>, Delphine Lagarde<sup>2</sup>, Andrea Balocchi<sup>2</sup>, Kenji Watanabe<sup>3</sup>, Takashi Taniguchi<sup>3</sup>, Xavier Marie<sup>2</sup>, Richard J. Warburton<sup>1,\*</sup>, Iann C. Gerber<sup>2,†</sup> and Bernhard Urbaszek<sup>2‡</sup>

<sup>1</sup>*Department of Physics, University of Basel, Basel, Switzerland*

<sup>2</sup>*Université de Toulouse, INSA-CNRS-UPS, LPCNO,  
135 Avenue Rangueil, 31077 Toulouse, France and*

<sup>3</sup>*National Institute for Materials Science, Tsukuba, Ibaraki 305-0044, Japan*

Transition metal dichalcogenides (TMDs) constitute a versatile platform for atomically thin optoelectronics devices and spin-valley memory applications. In monolayers optical absorption is strong, but the transition energy is not tunable as the neutral exciton has essentially no out-of-plane electric dipole. In contrast, interlayer exciton transitions in heterobilayers are widely tunable in applied electric fields, but their coupling to light is considerably reduced. Here, we show tuning over 120 meV of interlayer excitons with high oscillator strength in bilayer MoS<sub>2</sub>. These shifts are due to the quantum confined Stark effect, here the electron is localised to one of the layers yet the hole is delocalised across the bilayer. We optically probe the interaction between intra- and interlayer excitons as they are energetically tuned into resonance. This allows studying their mixing supported by beyond standard density functional theory calculations including excitonic effects. In MoS<sub>2</sub> trilayers our experiments uncover two types of interlayer excitons with and without in-built electric dipoles, respectively. Highly tunable excitonic transitions with large oscillator strength and in-built dipoles, that lead to considerable exciton-exciton interactions, hold great promise for non-linear optics with polaritons.

**Introduction.**— The optical properties of transition metal dichalcogenides (TMDs), such as MoS<sub>2</sub> and WSe<sub>2</sub>, are governed by excitons, Coulomb bound electron-hole pairs [1, 2]. High quality van der Waals heterostructures show close-to-unity, gate-tunable reflectivity of a single MoSe<sub>2</sub> layer [3, 4], variation of the transition energies of interlayer excitons over broad wavelength ranges in heterobilayers [5, 6] and valley polarized exciton currents [7].

In this work, we aim to combine the strong light-matter interaction of excitons in monolayers with high tunability of interlayer excitons in external electric fields. In heterobilayers the interlayer exciton is formed with the electron either in the top or in the bottom layer depending on the initial stacking [5]. Reports on interlayer excitons in heterobilayers rely mostly on photoluminescence emission [5–9] as interlayer absorption is very weak. In 2H stacked MoS<sub>2</sub> homobilayers, the situation is different. First, a strong feature in absorption up to room temperature, interpreted as an interlayer exciton, has been observed in earlier studies on MoS<sub>2</sub> bilayers [10–14]. Second, in principle, two energetically degenerate interlayer excitons can form with the electron residing in either the top or the bottom layer [15], whereas the hole is delocalized [16].

We integrate MoS<sub>2</sub> bilayers and trilayers in devices with top and bottom gates for applying a static out-of-plane electric field  $F_z$ . The energy degeneracy of the two interlayer exciton configurations is indeed lifted : In ab-

sorption, we observe two well-separated features as the amplitude of  $F_z$  is increased. This result reveals the large in-built electric dipole and proves the interlayer character of the transition. By adjusting  $F_z$ , we tune the energy splitting between the two interlayer excitons by as much as 120 meV, more than 10 times their linewidth. Essentially, no Stark shift is observable for the intralayer excitons A:1s and B:1s, as it is reported for monolayers [17, 18]. The interlayer character of the transitions is studied in applied magnetic fields showing large Zeeman splittings with opposite signs compared to intralayer transitions [19]. The red-shifted interlayer and the A-intralayer exciton show no clear mixing in absorption. In contrast, the blue-shifted interlayer exciton and the B-intralayer exciton exhibit an avoided crossing, indicating a mixing of these two states. The nature of this mixing is revealed in our calculations, showing that, with increasing  $F_z$ , the interlayer component in the B-intralayer exciton becomes stronger, and vice versa. In MoS<sub>2</sub> trilayers, we uncover different interlayer excitons with very distinct Stark shifts : Similar to the bilayer, one exciton splits into two resonances and shifts with electric field, indicating a large dipole. In contrast, a second type of the interlayer transition at lower energy shows a negligible Stark shift. According to our calculations, this particular transition shows a spatially symmetric charge distribution with respect to the middle layer and, hence, a negligible in-built dipole.

For optoelectronics, the highly tunable excitons with an in-built dipole found here in MoS<sub>2</sub> bilayers are promising for exploring coupling to optical cavity modes, where excitons and photons can couple to form polaritons [20, 21]. In III-V semiconductors very recently optical non-linearities at a single polariton level have been

\*Electronic address: richard.warburton@unibas.ch

†Electronic address: igerber@insa-toulouse.fr

‡Electronic address: urbaszek@insa-toulouse.fr

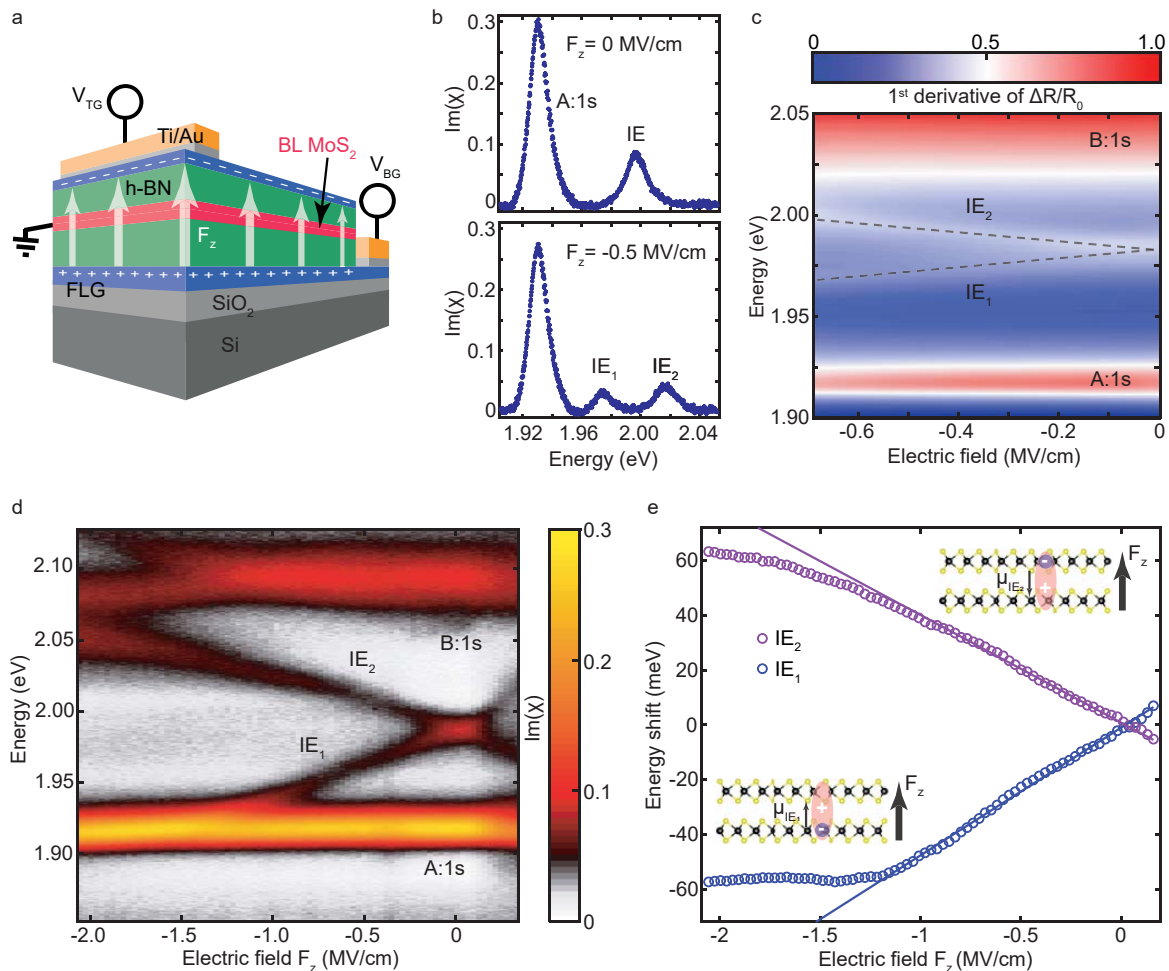


FIG. 1: **MoS<sub>2</sub> bilayer van der Waals heterostructure (vdWH) in an applied electric field** (all at  $T = 4$  K). **a**, Three-dimensional schematic of the device, consisting of a MoS<sub>2</sub> homobilayer encapsulated between two hexagonal boron nitride (hBN) flakes. Few-layer graphene (FLG) serves as top and bottom gate, while a direct Ti/Au contact to the MoS<sub>2</sub> is used to ground the bilayer. Voltages to the top and bottom gates ( $V_{TG}$  and  $V_{BG}$ ) are applied to create a uniform electric field  $F_z$  across the device. **b**, Typical absorption spectra recorded without ( $F_z = 0$  MV/cm) and with ( $F_z = -0.5$  MV/cm) an externally applied electric field, extracted from **d**. **c**, Stark shift of the interlayer excitons in a bilayer MoS<sub>2</sub> vdWH (device 2) at small electric fields. The intralayer A- and B-excitons (A:1s and B:1s) and the two branches of the interlayer A-resonances (IE<sub>1</sub> and IE<sub>2</sub>) are labelled. **d**, Colormap of the absorption spectra of bilayer MoS<sub>2</sub> (device 1) as a function of the electric field  $F_z$  applied perpendicular to the vdWH. **e**, Stark shift of the interlayer A-excitons as a function of  $F_z$ , extracted from the spectra in panel **d**. The solid blue and purple lines are linear fits to the experimental data points at small/moderate electric fields ( $F_z = 0.12$  MV/cm to  $F_z = -0.98$  MV/cm). Insets show the schematic of interlayer excitons in homobilayer MoS<sub>2</sub>. An electron localized in one layer interacts with a hybridized hole state to form an interlayer exciton. The direction of the dipole moment depends on the location of the electron, either in the bottom ( $\mu_{IE_1}$ ) or top ( $\mu_{IE_2}$ ) layer.

detected [22, 23]. Building on these promising proof-of-principle experiments further work on excitonic systems with stronger exciton-exciton interactions is desirable. This is the case for interlayer excitons in general in TMDs with in-built static dipole. The interlayer excitons in the homobilayers investigated here have the crucial advantage of a high oscillator strength.

**Stark effect tuning of interlayer excitons in bilayer MoS<sub>2</sub>.**— Our target is to identify the transitions in the MoS<sub>2</sub> bilayer absorption spectrum that carry an in-built out-of-plane electric dipole, and to tune their transition energy based on the the quantum confined

Stark effect [24]. Our experiments focus on momentum-direct intralayer and interlayer excitons in bilayer MoS<sub>2</sub> originating from valence and conduction bands around the  $K$ -point. Their strong oscillator strength results in very clear absorption signals and makes them relevant for room temperature experiments [13, 14]. We performed experiments as a function of the out-of-plane electric field in 2H stacked bilayer MoS<sub>2</sub> independently in two different research laboratories using devices 1 and 2, with a geometry as depicted in Fig. 1a : Two hexagonal boron nitride (hBN) flakes are used as dielectric spacers, and top and bottom few-layer graphene (FLG) act as trans-

parent electrodes (see Supplement for a description of the fabrication process). In device 1, a direct Ti/Au contact is added to the MoS<sub>2</sub> to operate the system in a dual-gate device scheme by grounding the bilayer, which allows independent control of the applied electric field and the carrier concentration. Applying a DC voltage to the top and bottom gate ( $V_{TG}$  and  $V_{BG}$ ) creates a uniform electric field in the MoS<sub>2</sub>, oriented perpendicular to the bilayer. The optical reflectivity was measured at low temperature ( $T = 4$  K) using a home-built confocal microscope and a weak, incoherent light source (see Supplement). The imaginary part of the optical susceptibility  $\text{Im}(\chi)$  was deduced from the differential reflectivity signal  $\Delta R/R_0$ ,  $\Delta R = R - R_0$ , using Kramers-Kronig relation, where  $R$  is the reflectivity spectrum obtained on the MoS<sub>2</sub> flake and  $R_0$  is the reference spectrum (see Supplement of [25] for a detailed description).

Fig. 1d shows typical absorption spectra as a function of the electric field  $F_z$ , recorded from device 1. Three prominent transitions can be clearly identified at zero electric field ( $F_z = 0$  MV/cm): The intralayer A- and B-exciton (A:1s and B:1s) near 1.93 eV and 2.10 eV, respectively, and the interlayer A-exciton (IE) at 2.00 eV [12]. When applying an external electric field  $F_z$ , the interlayer exciton (IE) splits into two separate branches, as seen in Fig. 1b for  $F_z = -0.5$  MV/cm. Using the area under the peaks in Fig. 1b as a rough measure of the relative absorption strength (we take A:1s as 100%), we see that at  $F_z = 0$  MV/cm the IE is about 30% compared to the intralayer A:1s state. Remarkably, at finite electric fields  $F_z = -0.5$  MV/cm the absorption strength does not vanish but remains rather strong, with a combined 24% from  $\text{IE}_1 + \text{IE}_2$  relative to the A:1s state. As  $F_z$  is increased, the energy difference between the  $\text{IE}_1$  and  $\text{IE}_2$  states reaches a value of  $\sim 120$  meV, covering a wide spectral range between the intralayer A- and B-exciton states.

For small to moderate electric fields, before significant interaction between the interlayer states and the A- and B-excitons, we observe a linear energy shift with  $F_z$  for both peaks,  $\text{IE}_1$  and  $\text{IE}_2$ , suggesting a first-order Stark shift caused by the static electric dipole moments across the MoS<sub>2</sub> bilayer (Fig. 1c,d). From fits of  $\Delta E$  versus  $F_z$  in the linear regime, large dipole moments of  $\mu_{\text{IE}_1} = (0.47 \pm 0.01) e\cdot\text{nm}$  and  $\mu_{\text{IE}_2} = (-0.39 \pm 0.01) e\cdot\text{nm}$  are extracted (Fig. 1e), with  $e$  being the electron charge. Our experiments clearly show that the absorption peak IE, initially at 2.00 eV, corresponds to interlayer exciton resonances with out-of-plane oriented electric dipoles as carriers do not reside within the same layer. For the intralayer excitons on the other hand, the energy shift with applied electric field is negligible, as in the case of excitons in monolayers [17, 18]. For the analysis of device 2, shown in Fig. 1c, we extract a dipole value with a lower bound of about  $0.3 e\cdot\text{nm}$ . In terms of order of magnitude, the large extracted dipole moments are very similar to results on interlayer excitons in MoSe<sub>2</sub>/WSe<sub>2</sub> *heterobilayers* using photoluminescence [5–7, 26]. For comparison

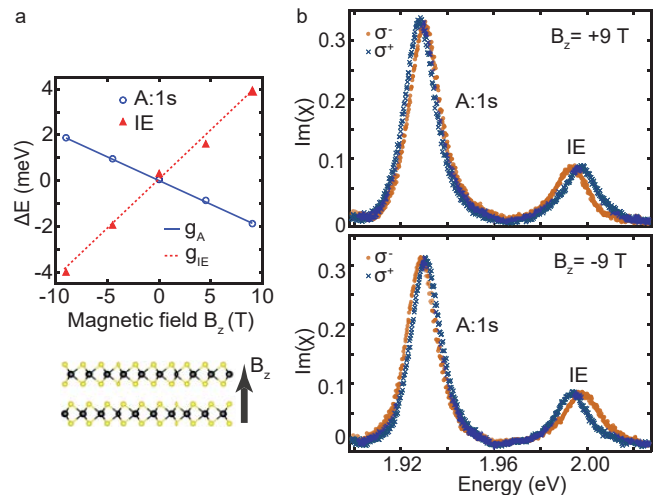


FIG. 2: **Magneto-optics at zero electric field ( $F_z = 0$  MV/cm).** **a**, Energy difference  $\Delta E$  between the two circular polarizations for the intralayer (blue) and interlayer (red) A-exciton at different magnetic fields  $B_z$ . The  $g$ -factors of the two transitions are extracted from linear fits. The intralayer A-exciton has a negative  $g$ -factor,  $g_A = -3.6 \pm 0.1$ , while the interlayer excitonic  $g$ -factor is approximately twice as large with opposite sign,  $g_{\text{IE}} = 7.4 \pm 1.1$ . The errors in the  $g$ -factors represent a 95% confidence interval that is calculated from the uncertainty of the fitting parameter (see Supplement). **b**, Polarization-resolved absorption spectra for bilayer MoS<sub>2</sub> in positive and negative magnetic fields ( $B_z = +9$  T and  $B_z = -9$  T) applied perpendicular to the layers. The orange and blue curves correspond to  $\sigma^-$  and  $\sigma^+$ -polarization.

with other *homobilayer* systems, interlayer excitons have very different characteristics depending on the TMD material [27, 28]. For WSe<sub>2</sub> bilayers, reports on interlayer excitons focus on transitions indirect in momentum space linked to the indirect band gap energetically below the direct  $K$ - $K$  transitions [29, 30]. In the case of MoSe<sub>2</sub>,  $K$ - $K$  interlayer excitons are observed with similarities to the case of MoS<sub>2</sub>, but with significantly lower oscillator strength [31–33]. This is mainly due to the larger valence band spin-orbit splitting of MoSe<sub>2</sub> compared to MoS<sub>2</sub>, which makes hole delocalization over both layers and hence the formation of interlayer excitons less favourable [16].

**Zeeman splitting of interlayer excitons.**— Magneto-optics is a powerful tool for line identification and transition energy tuning [26]. The A-intralayer exciton, which exhibits a negligible Stark shift, shows a negative Zeeman splitting of about 2 meV at  $B_z = +9$  T, which changes sign as the magnetic field direction is reversed in Fig. 2a and b. We deduce a negative Landé  $g$ -factor of around  $-3.6$  for the intralayer exciton A:1s [10]. The Zeeman splitting for interlayer excitons is about 4 meV at  $B_z = +9$  T, and the sign is opposite compared to the intralayer case. We deduce a  $g$ -factor of about  $g_{\text{IE}} \approx 7.4$  from the data presented in Fig. 2. The larger Zeeman splitting with opposite sign compared to

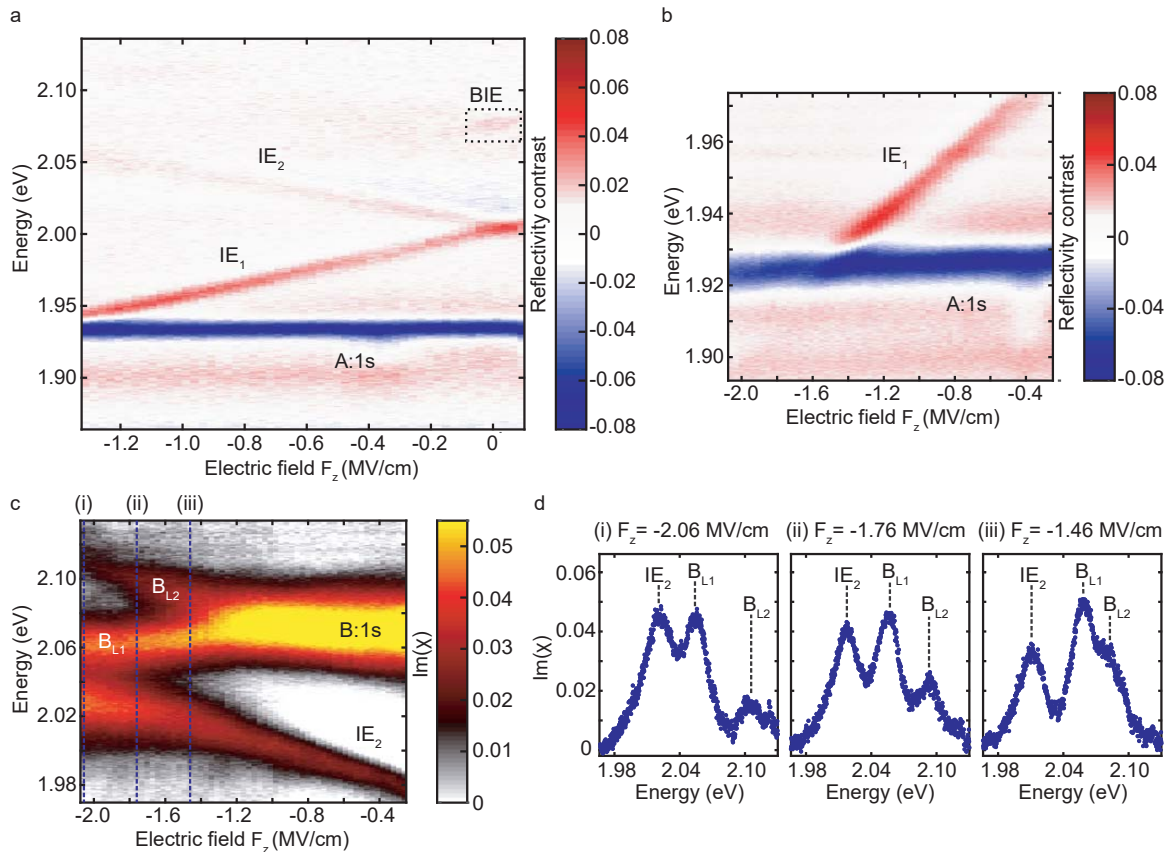


FIG. 3: **Electric field dependence in a magnetic field ( $B_z = +9$  T).** **a**, Colormap of the differential reflectivity contrast between  $\sigma^+$ - and  $\sigma^-$ -polarization ( $\Delta R/R_0(\sigma^+) - \Delta R/R_0(\sigma^-)$ ) at  $B_z = +9$  T on applying an external electric field across the MoS<sub>2</sub> bilayer. A negative value, corresponding to a dip in the differential reflectivity spectrum, reflects a negative  $g$ -factor, while a positive value reflects a positive  $g$ -factor. In this panel, we can also observe a transition  $\sim 30$  meV below the intralayer B-exciton (at  $F_z = 0$  MV/cm), labelled as BIE. Its positive  $g$ -factor as well as its tunability with electric field clearly indicate an interlayer character [10]. **b**, Zoom into the lower energy region with the interlayer exciton IE<sub>1</sub> approaching the A-exciton. At an electric field of  $F_z \approx -1.43$  MV/cm, the interlayer exciton merges into the intralayer A-exciton; there is no evidence of any crossing or anticrossing of the two resonances. **c**, Colormap of the absorption spectra ( $\sigma^+$ -polarization) centered around the intralayer B-exciton, demonstrating a strong interaction between the two excitonic states. At  $F_z \approx -1.43$  MV/cm, the interlayer exciton IE<sub>2</sub> anticrosses with B<sub>L2</sub>, while the intralayer resonance B<sub>L1</sub> remains unaffected. This is shown in **d** by individual absorption spectra at different electric fields, as marked by dashed lines (i)-(iii) in **c**.

intralayer excitons has been observed for other multilayer systems [19]. The spin contributions to the Zeeman splitting for an optical transition within the same layer cancel (at least partially) for intralayer excitons, whereas they are additive for interlayer excitons. For interlayer excitons, Stark effect tuning over tens of meV could therefore be combined in principle with an additional magnetic field splitting of the two interlayer Zeeman states. Our knowledge about interlayer versus intralayer magneto-optics will also be crucial for discussing the trilayer results below.

**Tuning interlayer and intralayer absorption into resonance.**— Due to the very large tunability shown in Fig. 1 for the interlayer exciton transition energy, we are able to tune the interlayer excitons into resonance with the intralayer states. Fig. 3a maps the differential reflectivity contrast between  $\sigma^+$ - and  $\sigma^-$ -

polarization ( $\Delta R/R_0(\sigma^+) - \Delta R/R_0(\sigma^-)$ ) at  $B_z = 9$  T when applying an external electric field across the MoS<sub>2</sub> bilayer. As discussed above, intra- and interlayer transitions show opposite  $g$ -factors, being reflected by negative and positive values in the reflectivity contrast (see Supplement measurements at  $B_z = 0$  T).

Zooming into the low-energy region (Fig. 3b) shows that there is no clear signature of an interaction between the intralayer A-exciton and the lower interlayer branch; the IE<sub>1</sub> state seems to merge into its intralayer counterpart (see Supplement for single spectra at selected field values). We do not observe any clear crossing or anticrossing in our reflection contrast measurements. From an experimental point of view, we therefore conclude that, in the devices investigated, we are unable to tune the interlayer exciton energy below the A-intralayer transition energy while keeping a strong optical oscillator

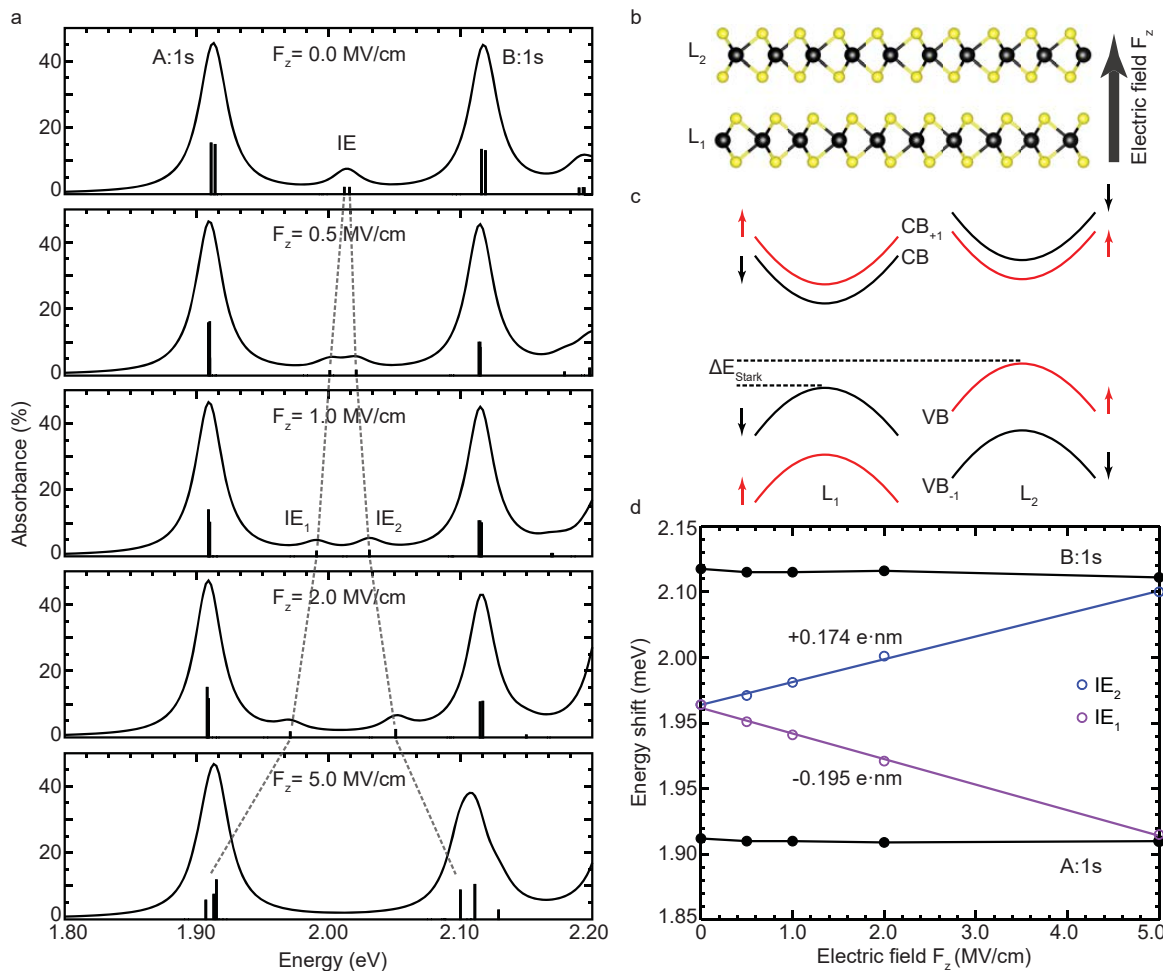


FIG. 4: **Beyond-DFT calculations of the electric field effects on the band structure and excitonic properties of 2H MoS<sub>2</sub> bilayer.** **a**, Absorbance spectra as a function of the applied electric field  $F_z$ . **b**, Structural model of the 2H bilayer stacking and electric field direction. **c**, Schematic of the band structure modification due to the application of  $F_z$ , showing a global shift, denoted  $\Delta E_{\text{Stark}}$ , between the distinct band structures of the two layers (see Supplement for detailed results on *GW* band structure calculations). **d**, Evolution of the excitonic peak positions with respect to the electric field, and the corresponding dipole estimates for IE<sub>1</sub> and IE<sub>2</sub> excitons.

strength.

However, tuning the upper interlayer branch IE<sub>2</sub> energetically close to resonance with the B-exciton leads to an avoided crossing (Fig. 3c). Looking at the data in detail, we see that the broad B-exciton splits into two resonances associated to intralayer excitons in the two different layers, labelled as B<sub>L1</sub> and B<sub>L2</sub> in Fig. 3c, where we denote layer 1 (L<sub>1</sub>) and layer 2 (L<sub>2</sub>). Only B<sub>L2</sub> shifts towards higher energies as the IE<sub>2</sub> approaches, the transition B<sub>L1</sub> remains largely unaffected, as can be seen from the individual spectra in Fig. 3d. Our experiments therefore suggest a strong interaction between the IE<sub>2</sub> and B<sub>L2</sub> transitions (see discussion in the theory section).

**GW+BSE modeling of excitons in MoS<sub>2</sub> bilayers.**— The main observations of the experiments on devices 1 and 2 are (i) the splitting and very large shift of the IE transition in an applied electric field, (ii) anticrossing of the IE<sub>2</sub> with the B-intralayer exciton and

(iii) no clear crossing of the IE<sub>1</sub> with the A-intralayer exciton. We have performed *GW*+BSE calculations to develop a qualitative understanding of the observed effects. Our approach is based on the inclusion of the applied electric field as a perturbation in the band structure calculations (see Supplement for computational details). Please note that we have only considered freestanding 2H MoS<sub>2</sub> bilayers in our calculations, *i.e.* placed in vacuum, as we aim to reproduce qualitatively the main trends. When applying an electric field [34], we observe a global shift of the relevant conduction and valence bands at the *K*-point down in energy marked as  $\Delta E_{\text{Stark}}$ , for L<sub>1</sub> with respect to L<sub>2</sub> (see Fig. 4b for the electric field configuration and Fig. 4c for a band structure schematic). Please also see Supplement for a more realistic *GW* picture of this effect on the band structures. From the sketch in Fig. 4c it is thus clear that the IE transitions will split in energy: Transitions involving the L<sub>2</sub> valence bands and

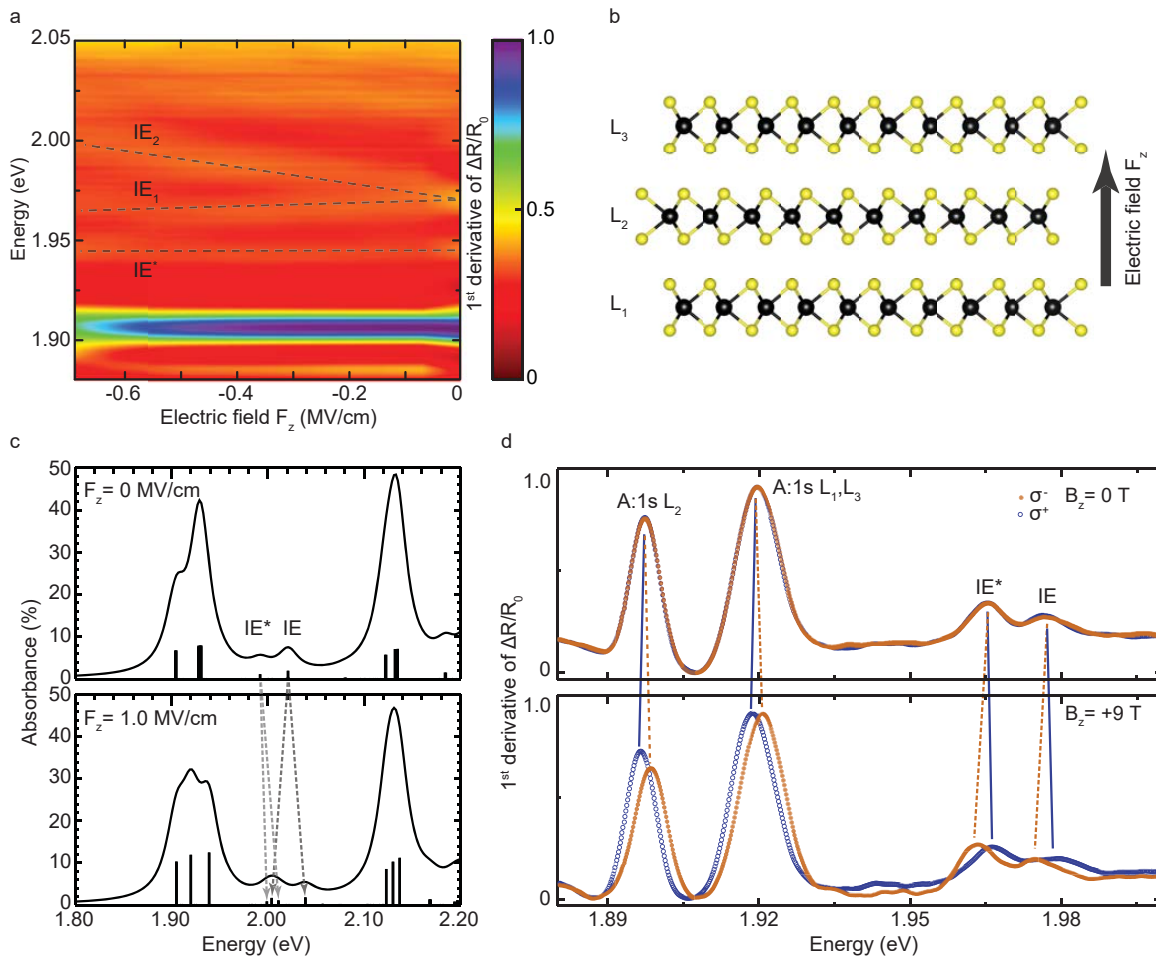


FIG. 5: **MoS<sub>2</sub> trilayer in an applied electric field.** **a**, Colormap of the normalized reflectivity contrast. **b**, Schematic of 2H stacked trilayer studied. **c**, Theoretical absorption spectra of 2H MoS<sub>2</sub> freestanding trilayer without (top) and with (bottom) electric field. See Supplement for a detailed discussion of the trilayer band structure and the effect of the electric field on it. The Stark shifts of interlayer excitons IE and IE\* are indicated by arrows. **d**, Magneto-optics with small Zeeman splitting for intralayer excitons (A:1s) and large Zeeman splitting for interlayer excitons IE and IE\* in magnetic fields of 9 T perpendicular to the monolayer plane.

the conduction bands in L<sub>1</sub> will lower in energy, whereas transitions involving the L<sub>1</sub> valence bands and L<sub>2</sub> conduction bands will increase in energy.

After including excitonic effects, we are able to calculate the absorption (in Fig. 4a) which looks very similar to our measurements (see Fig. 1b). Fig. 4d demonstrates how the IE transition energy changes, roughly linearly, with the applied electric field. At large electric field values of 5 MV/cm, we see two main groups of transitions: At the low energy side, the IE<sub>1</sub> close to the A-exciton energy and, at the high energy side, the IE<sub>2</sub> close to the B-exciton. There is essentially no transitions in the energy range in-between. We refrain in our calculations to comment on any higher electric field values as our initial assumption to treat the electric field as a perturbation, in comparison with other energy splittings in the band structure, reaches its limits.

The exact nature and mixing of the absorption peaks,

calculated in Fig. 4a, contains information on the evolution of the exciton states with electric field (see Supplement for summary tables). We can use this knowledge to analyze the results in Fig. 3b and c in particular: For finite electric fields, the intralayer A-exciton contains a very small IE component that remains small as the field increases. Our theory indicates very little mixing between the A-intralayer exciton and the IE, which is consistent with the experiments in Fig. 3b. Concerning interactions with the intralayer B-exciton, the IE exciton, with the hole delocalized, is mixed with the intralayer B-exciton as they share the same valence states. This was suggested in [12] to explain the surprisingly high oscillator strength of the IE transitions. In our calculations, we see that the mixing between the higher energy IE branch and the B-exciton becomes stronger as the electric field amplitude is increased (see Supplement for a detailed description of each oscillator strength decomposition). We

suggest that this clear trend from our calculations is at the origin of the observed anti-crossing between  $IE_2$  and  $B_{L_2}$  shown in Fig. 3c.

Our  $GW+BSE$  calculations therefore capture the main experimental findings - the observed IE Stark shift and the interactions with intralayer A- and B-exciton resonances.

**Interlayer excitons in MoS<sub>2</sub> trilayers.**— After detailed studies of the bilayer physics, we also worked on the excitonic transitions in trilayer MoS<sub>2</sub> as part of the same device (device 2). At zero electric field, two different interlayer transitions appear in absorption, labelled  $IE^*$  and  $IE$  in Fig. 5. We show absorption measurements as a function of the electric field and make a surprising observation : Whereas  $IE$  splits into two branches ( $IE_1$  and  $IE_2$ ) as for the bilayer studies,  $IE^*$  does not show any measurable splitting and hence, a negligible in-built electric dipole moment. Interestingly, we make the same observation in our  $GW+BSE$  calculations, shown in Fig. 5c. The absence of a clear Stark shift might put the interlayer nature of  $IE^*$  into question . To answer this, we have performed magneto-optics, shown in Fig. 5d. We observe for the intralayer excitons a Zeeman splitting of the order of 2 meV for  $B_z = 9$  T and for  $IE$  and  $IE^*$ , a Zeeman splitting of the order of 4 meV, with opposite sign compared to the intralayer transitions. Therefore, we confirm the interlayer character of those peaks (see also [10]). These results lead to an unusual situation for interlayer excitons : We observe a strong splitting in magnetic fields for  $IE^*$ , but a very small Stark shift in electric fields. This can be explained by the microscopic origin of  $IE^*$  obtained from our calculations : For  $IE^*$ , the electron is localized in the middle layer ( $L_2$ ) and the hole is delocalized almost evenly over the other two layers ( $L_{1,3}$ ), mediated by an small intralayer contribution. This symmetric charge carrier distribution results in a negligible net dipole. In contrast, the trilayer  $IE$  at higher energy consists of a localized hole in  $L_2$ , which interacts preferentially with an electron in one of the two layers  $L_1$  or  $L_3$ . This results in two possible  $IE$  configurations. The  $IE$ , consisting of a hole in  $L_2$  interacting with an electron in  $L_3$ , and the  $IE$  configuration with the hole still in  $L_2$  but the electron mainly in  $L_1$  (see Supplement). Both configurations carry a net dipole which results in a measurable Stark splitting of the  $IE$  transition in Fig. 5.

## I. SUPPLEMENTARY INFORMATION

### A. Sample fabrication

Van der Waals heterostructures (vdWHs) were fabricated by stacking two-dimensional materials via dry-transfer techniques. Two separate devices were fabricated : Device 1 was prepared at the University of Basel and device 2 was assembled at LPCNO Toulouse. For device 1, a polydimethylsiloxane (PDMS) stamp with a thin polycarbonate (PC) film was used to pick up individ-

ual layers from top to bottom. All flakes were previously mechanically exfoliated from bulk crystals (natural MoS<sub>2</sub> crystal from SPI Supplies, synthetic hexagonal boron nitride (hBN) [35], and natural graphite from Graphene Supermarket) on SiO<sub>2</sub> (300 nm)/Si substrates. Metal contacts to the MoS<sub>2</sub> and few-layer graphene (FLG) were patterned by electron-beam lithography and subsequent metal deposition of Ti(5 nm)/Au (45 nm). For device 2, 2H-MoS<sub>2</sub> crystals (2D Semiconductors), synthetic hBN [35] and natural graphite were subjected to micromechanical cleavage on Nitto Denko tape [36], then exfoliated again on a PDMS stamp placed on a glass slide for optical inspection. Sequential deterministic stamping of the selected flakes was then applied to build the complete stack, aligned according to the position of the Au contacts pre-patterned onto the substrate. Optical images of both devices (1 and 2) are shown in Fig. 7a (left and right). The thicknesses of the individual hBN layers were measured by atomic force microscopy ( $d_T = 16.2$  nm and  $d_B = 21.5$  nm for device 1, and  $d_T = 13$  nm and  $d_B = 4$  nm for device 2).

### B. Experimental setups

The reflectivity spectra of device 1 were recorded with the setup sketched in Fig. 6. A white light emitting diode (LED) is coupled into a multi-mode fiber, with its output connected to a home-built microscope. The incoming light is first sent through a linear polarizer. A computer controlled liquid crystal (LC) retarder that can create a  $+\lambda/2$  or  $-\lambda/2$  retardance of the initial beam is used to produce two perpendicular linear polarizations on demand. An achromatic quarter-wave plate retarder ( $\lambda/4$ ) is subsequently used to circularly polarize the light. By controlling the voltage on the LC retarder, the incoming LED light can thus be circularly polarized with either right- ( $\sigma^+$ ) or left- ( $\sigma^-$ ) handed orientation. The light then passes into a helium bath cryostat where it is focused onto the sample at 4.2 K using a microscope objective (NA = 0.45). The position of the sample with respect to the focus can be adjusted with cryogenic nanopositioners. The reflected light from the sample is coupled into a single-mode fiber, ensuring a confocal detection, and sent to a spectrometer with a 600 grooves per millimeter grating. The spectra are recorded by a liquid-nitrogen cooled charged coupled device (CCD) array.

In order to evaluate the differential reflectivity  $\Delta R/R_0$ , we compare the reflectivity spectrum  $R$  obtained from the MoS<sub>2</sub> flake at a given electric field  $F_z$  with a reference spectrum  $R_0$ . Sweeping the gate voltages  $V_{TG}$  and  $V_{BG}$  so that only the carrier concentration  $n_{tot}$  in the device is varied leads to significantly different reflectivity spectra. For device 1, we thus extrapolate the reference spectrum  $R_0$  from the raw reflectivity spectrum at a high electron density  $n_{tot} \approx 11.5 \cdot 10^{-12}$  cm<sup>-2</sup>, where the oscillator strength is distributed over a large spectral range [37]. Using Kramers-Kronig relation, the measured dif-

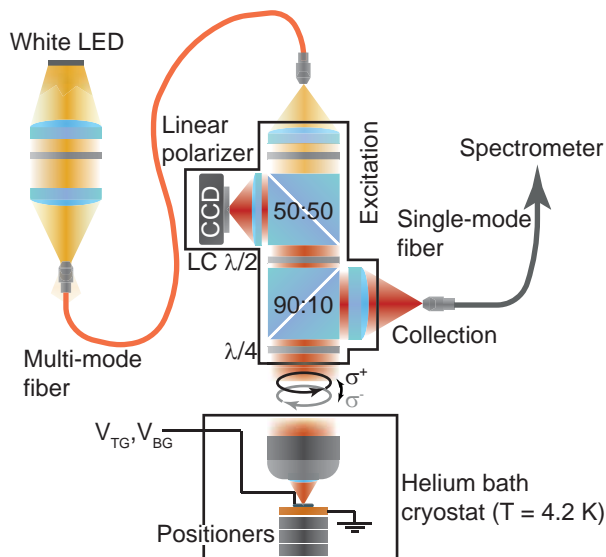


FIG. 6: **Experimental setup.**

ferential reflectivity data  $\Delta R/R_0$  can be converted into the imaginary part of the optical susceptibility  $\text{Im}(\chi)$  (see also Supplement of [25] for a more detailed description).

For device 2, low temperature reflectance measurements were performed in a home-built microspectroscopy setup constructed around a closed-cycle, low vibration attoDry cryostat with a temperature controller ( $T = 4 \text{ K}$  to  $T = 300 \text{ K}$ ). For reflectivity, a halogen lamp with a stabilized power supply is used as a white light source, initially focused onto a pin-hole that is imaged on the sample. The reflected light is then dispersed by spectrometer and detected by a Si-CCD camera. Here, the differential reflectivity is defined as  $\Delta R/R_0$ , where  $R$  is the intensity reflection coefficient of the sample with the MoS<sub>2</sub> layers and  $R_0$  is obtained from the same structure without the MoS<sub>2</sub>. Note that the overall shape and amplitude of the differential reflectivity signal depends on thin-film interferences in the hBN layers [38].

### C. Electrostatic model

The presence of the (optical transparent) top and bottom electrical gates, in addition to the directly contacted MoS<sub>2</sub> bilayer (in device 1), allow us to control the total carrier density  $n_{\text{tot}}$  of the MoS<sub>2</sub> bilayer as well as the electric field  $F_z$  across the heterostructure using the voltages  $V_{\text{TG}}$  and  $V_{\text{BG}}$  applied to the top and bottom gates.

We consider the electrostatic model schematically depicted in Fig. 7b (see also Main Fig. 1a). The MoS<sub>2</sub> bilayer is modelled as two grounded conducting plates in between two two insulating hBN layers. Upon electrical

gating, top and bottom displacement fields,  $D_{\text{T}}$  and  $D_{\text{B}}$ , respectively, lead to a net carrier doping  $n_{\text{tot}}$  of the MoS<sub>2</sub> bilayer, as well as an imposed interlayer electric field  $D$ . By setting  $n_{\text{tot}}$  and varying  $D$ , we can tune the interlayer electric field while keeping the carrier concentration in the MoS<sub>2</sub> bilayer constant. By varying  $n_{\text{tot}}$  above or below zero, we can inject electrons or holes into the bilayer and shift the Fermi level without changing the electric field across the heterostructure.

In our experiment, the displacement fields  $D_{\text{T}}$  and  $D_{\text{B}}$  are tuned independently by the top and bottom gate voltages, through the relations

$$D_{\text{T}} = C_{\text{T}}(V_{\text{TG}} - V_{\text{TG}}^0) \quad (1)$$

$$\text{and } D_{\text{B}} = -C_{\text{B}}(V_{\text{BG}} - V_{\text{BG}}^0). \quad (2)$$

Here,  $V_{\text{TG}}$  and  $V_{\text{BG}}$  are the voltages applied to the top and bottom gates, and  $V^0$  is the effective offset voltage due to initial environmental carrier doping. To describe the capacitive system, we introduce the relevant geometric top and bottom gate capacitances per unit area as

$$C_{\text{T}} = \frac{\epsilon_0 \epsilon_{\text{hBN}}}{d_{\text{T}}} \quad \text{and} \quad C_{\text{B}} = \frac{\epsilon_0 \epsilon_{\text{hBN}}}{d_{\text{B}}}. \quad (3)$$

Here,  $d_{\text{T}} = 16.2 \text{ nm}$  and  $d_{\text{B}} = 21.5 \text{ nm}$  are the thicknesses of the top and bottom hBN layers (in device 1) as determined by AFM measurements,  $\epsilon_0$  is the vacuum permittivity and  $\epsilon_{\text{hBN}} \approx 3.76$  [39] is the dielectric constant of hBN. Using the plate capacitor model, we can define the total applied electron density as

$$\begin{aligned} n_{\text{tot}} &= n_{\text{T}} + n_{\text{B}} \\ &= \frac{1}{e} [C_{\text{T}}(V_{\text{TG}} - V_{\text{TG}}^0) + C_{\text{B}}(V_{\text{BG}} - V_{\text{BG}}^0)], \end{aligned} \quad (4)$$

where  $n_{\text{T}}$  and  $n_{\text{B}}$  are the carrier densities in the top and bottom layers, and  $e$  is the electron charge. From Eq. 3 and 4, the net carrier doping can be calculated to be

$$n_{\text{tot}} = \frac{1}{e} \frac{\epsilon_0 \epsilon_{\text{hBN}}}{d_{\text{T}}} \left[ (V_{\text{TG}} - V_{\text{TG}}^0) + \frac{d_{\text{T}}}{d_{\text{B}}} (V_{\text{BG}} - V_{\text{BG}}^0) \right]. \quad (5)$$

Now, we evaluate quantitatively the electric displacement in the system, assuming that there are no charges accumulated at the interfaces

$$\begin{aligned} D &= \frac{1}{2} [C_{\text{T}}(V_{\text{TG}} - V_{\text{TG}}^0) - C_{\text{B}}(V_{\text{BG}} - V_{\text{BG}}^0)] \\ &= \frac{1}{2} \epsilon_0 \epsilon_{\text{hBN}} \left[ \frac{(V_{\text{TG}} - V_{\text{TG}}^0)}{d_{\text{T}}} - \frac{(V_{\text{BG}} - V_{\text{BG}}^0)}{d_{\text{B}}} \right]. \end{aligned} \quad (6)$$

The electric field across the bilayer MoS<sub>2</sub> can then be calculated to be

$$F_z = \frac{1}{2} \frac{\epsilon_{\text{hBN}}}{\epsilon_{\text{BL}} d_{\text{B}}} \left[ (V_{\text{TG}} - V_{\text{TG}}^0) - \frac{d_{\text{T}}}{d_{\text{B}}} (V_{\text{BG}} - V_{\text{BG}}^0) \right], \quad (7)$$

where we used  $D = \epsilon_0 \epsilon_{\text{BL}} F_z$ , with  $\epsilon_{\text{BL}} \approx 6.8$  [39] being the dielectric constant of bilayer MoS<sub>2</sub>.

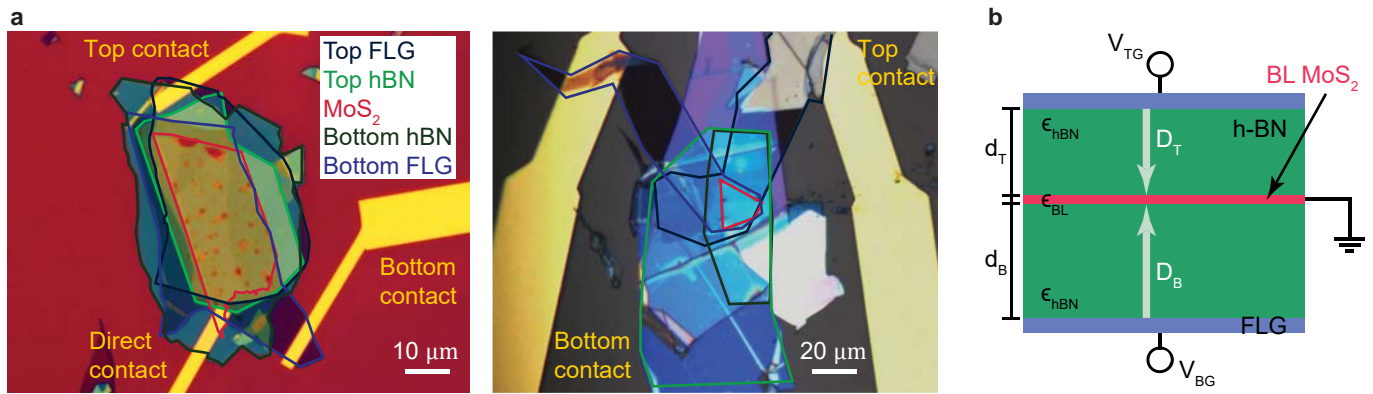


FIG. 7: **Device structure.** **a**, Microscope images of device 1 (left) and device 2 (right). **b**, Schematic of the electrostatic model.

From constant absorption at the A:1s intralayer exciton resonance, we can confirm that, for the applied top and bottom gate voltages, our gate operation scheme (in device 1) only varies the electric field  $F_z$ , while the carrier concentration in the MoS<sub>2</sub> bilayer stays constant.

## D. Magnetic field dependence

### 1. Zeeman splitting

Applying a magnetic field  $B_z$  perpendicular to the sample plane lifts the valley degeneracy (valley Zeeman

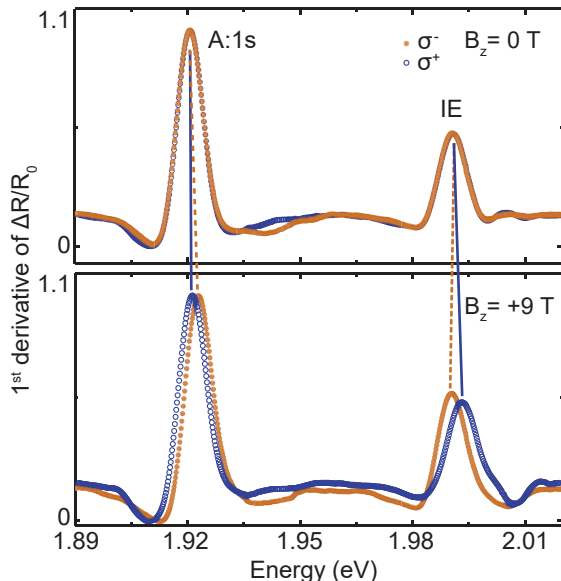


FIG. 8: **Polarization-resolved absorption spectra of bilayer MoS<sub>2</sub> (device 3) at  $B_z = 0$  T (top) and  $B_z = +9$  T (bottom).** The orange and blue curves correspond to  $\sigma^-$ - and  $\sigma^+$ -polarization. Intra- and interlayer A-excitons (A:1s and IE) are labelled.

effect) and allows the measurement of the intra- and interlayer exciton  $g$ -factor. The Zeeman splittings of the two excitonic transitions, A:1s and IE, are defined as  $\Delta E_A = E(\sigma^+) - E(\sigma^-) = g_A \mu_B B_z$  and  $\Delta E_{IE} = g_{IE} \mu_B B_z$  with  $E(\sigma^+)$  and  $E(\sigma^-)$  being the transition energies for the two circular polarizations,  $g_A$  and  $g_{IE}$  are the excitonic  $g$ -factors, and  $\mu_B = 58 \mu\text{eV/T}$  is the Bohr's magneton. The  $g$ -factors  $g_A$  and  $g_{IE}$  in Main Fig. 2a are obtained from linear fits of  $\Delta E$  versus  $B_z$ , divided by  $\mu_B$ . Fig. 8 shows polarization-resolved absorption spectra of a third bilayer MoS<sub>2</sub> sample (device 3), fabricated at LPCNO Toulouse, at  $B_z = 0$  T and  $B_z = +9$  T. In agreement with device 1, built at University of Basel, (see Main Fig. 2), the interlayer exciton IE exhibits a larger Zeeman splitting with opposite sign compared to the intralayer exciton A:1s. Fig. 8 (top) further confirms that there is no difference between the two circular polarizations ( $\sigma^+$ - and  $\sigma^-$ ) at  $B_z = 0$  T.

### 2. Differential reflectivity contrast

The reflectivity contrast, constructed as the difference between the differential reflectivity spectra recorded for  $\sigma^+$ - and  $\sigma^-$ -polarization ( $\Delta R/R_0(\sigma^+) - \Delta R/R_0(\sigma^-)$ ), gives information about the  $g$ -factors (sign and amplitude) of the individual resonances. As can be deduced from our polarization-resolved absorption measurements (see Main Fig. 3 and also Fig. 8), dips in the reflectivity contrast spectra correspond to excitonic resonances with negative  $g$ -factors ( $g < 0$ ), positive values are related to resonances exhibiting a positive  $g$ -factor ( $g > 0$ ). Fig. 9 shows the full absorption (top) and differential reflectivity contrast spectrum (bottom) at zero electric field ( $F_z = 0$  MV/cm), extracted from the colormap in Main Fig. 3a. Four resonances can be observed, identified as the intralayer A:1s and B:1s excitons (with negative  $g$ -factors) and the interlayer IE and BIE excitons (with positive  $g$ -factors).

In Fig. 10, absorption and differential reflectivity con-

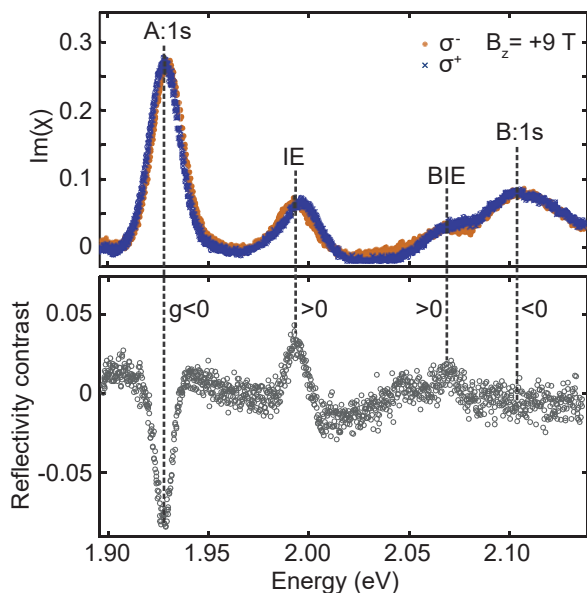


FIG. 9: **Absorption and differential reflectivity contrast at zero electric field ( $F_z = 0$  MV/cm).** Absorption (top) and differential reflectivity contrast ( $\Delta R/R_0(\sigma^+) - \Delta R/R_0(\sigma^-)$ ) spectrum (bottom) of homobilayer MoS<sub>2</sub> (device 1) at  $B_z = +9$  T without an externally applied electric field ( $F_z = 0$  MV/cm). The intralayer A- and B-excitons (A:1s and B:1s) and the two interlayer A- and B-resonances (IE and BIE) are labelled. Dips in the reflectivity contrast indicate a negative  $g$ -factor (blue in the colormap in Main Fig. 3a), while peaks indicate a positive  $g$ -factor (red in the colormap in Main Fig. 3a) of the excitonic transition.

trast spectra (extracted from the colormap in Main Fig. 3b) are depicted for the situation (iii) before, (ii) while and (i) after the intralayer A:1s and interlayer IE<sub>1</sub> exciton are energetically tuned into resonance. At  $F_z = -1.94$  MV/cm, the dip in the reflectivity contrast spectrum for the A:1s transition is less pronounced compared to the one at  $F_z = -0.98$  MV/cm; the intralayer  $g$ -factor amplitude decreases when the interlayer IE<sub>1</sub> transition “merges” into the intralayer A:1s transition.

## E. Beyond-DFT calculations

### 1. Computational details

The atomic structures, the quasi-particle band structures and optical spectra have been obtained from DFT calculations using the VASP package [40, 41]. The plane-augmented wave scheme [42, 43] has been used to treat core electrons. We have set the lattice parameter value of 3.22 Å for all the runs. A grid of  $15 \times 15 \times 1$  k-points has been used, in conjunction with a vacuum height of 21.9 Å, for all the calculation cells. The geometry’s optimization process has been performed at the PBE-D3 level [44] in order to include van der Waals interactions between layers. All the atoms were allowed to relax with

a force convergence criterion below 0.005 eV/Å. Heyd-Scuseria-Ernzerhof (HSE) hybrid functional [45–47] has been used as approximation of the exchange-correlation electronic term, including SOC, to determine eigenvalues and wave functions as input for the full-frequency-dependent  $GW$  calculations [48] performed at the  $G_0W_0$  level. The application of the electric field is done at this step, just before the  $GW$  calculation process, considering that at small/moderate electric field values, its application is only a small perturbation to the band structures. An energy cutoff of 400 eV and a Gaussian smearing of 0.05 eV width have been chosen for partial occupancies, when a tight electronic minimization tolerance of  $10^{-8}$  eV was set to determine, with a good precision, the corresponding derivative of the orbitals with respect to  $k$  needed in quasi-particle band structure calculations. The total number of states included in the  $GW$  procedure is set to 1280, in conjunction with an energy cutoff of 100 eV for the response function, after a careful check of the direct band gap convergence (smaller than 0.1 eV as a function of k-points sampling). Band structures have been obtained after a Wannier interpolation procedure performed by the WANNIER90 program [49]. All optical excitonic transitions have been calculated by solving the Bethe-Salpeter Eq. [50, 51], using the twelve highest valence bands and the sixteen lowest conduction bands to obtain eigenvalues and oscillator strengths on all systems. From these calculations, we report the absorbance values by using the imaginary part of the complex dielectric function.

### 2. Band structure modifications due to the electric field

As can be seen in Fig. 11, moderate electric field application on a free standing 2H MoS<sub>2</sub> bilayer shifts band structures from the two distinct layers by decreasing valence bands and conduction band energies for the layer L<sub>1</sub> lying at the highest electrostatic potential value while L<sub>2</sub> bands are upshifted. Mind that similar results were already reported in previous works using standard DFT calculations only [52–54], confirmed here by our  $GW$  series of calculations.

In Fig. 12, the band structures of the trilayer case are reported. Interestingly, without electric field, L<sub>1</sub> and L<sub>3</sub> valence bands, more specifically VB and VB<sub>-1</sub>, are both mixtures of Mo  $d_{xy}$ ,  $d_{x^2-y^2}$  with in-plane S  $p$  orbitals coming from both L<sub>1</sub> and L<sub>3</sub> layers. Thus, when making transitions implying those states (solid black lines in Fig. 12), holes will be delocalized over the top and bottom layers at the same time. By suppressing symmetry, with the application of an electric field, VB and VB<sub>-1</sub> become more relocalized one each of the layers. Since our calculation cell is symmetric in the ( $Oz$ ) direction, and since L<sub>2</sub> is located in the middle of it, its corresponding electrostatic potential is 0. This explains the absence of band shifts for the L<sub>2</sub> bands.

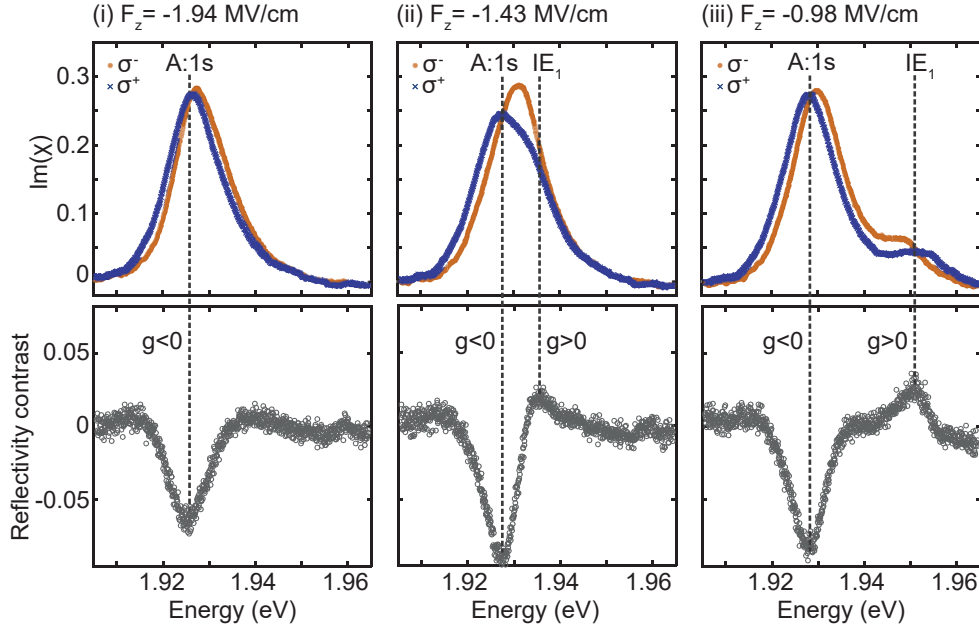


FIG. 10: **Absorption and differential reflectivity contrast at different electric fields.** Absorption (top) and differential reflectivity contrast ( $\Delta R/R_0(\sigma^+) - \Delta R/R_0(\sigma^-)$ ) spectra (bottom) for selected electric field values as the interlayer  $IE_1$  and intralayer A:1s exciton are energetically tuned into resonance (see colormap in Main Fig. 3b).

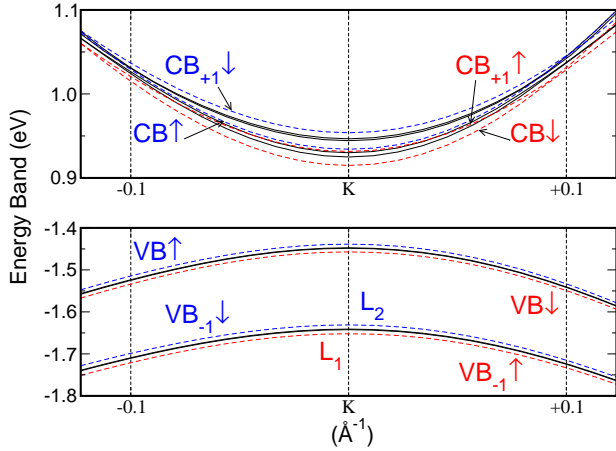


FIG. 11: **Valence and conduction bands shifts induced by an electric field.**  $G_0W_0$  band structure of 2H MoS<sub>2</sub> bilayer in the vicinity of the K-point, without (black lines) and with an applied electric field  $F_z = 1$  MV/cm value (dashed lines).  $L_1$  bands are in red, while  $L_2$  bands are depicted in blue.

### 3. Decomposition of the exciton oscillator strength with respect to single particle transitions : Bilayer case

From Table I, one can see that the A-exciton is not completely of pure intralayer exciton character, since a small amount (around 5%) of the oscillator strength is coming from the  $VB_{-1}$  of the other layer. This mixing does not vary with respect to the electric field. Note that no delocalization of the electron, as expected

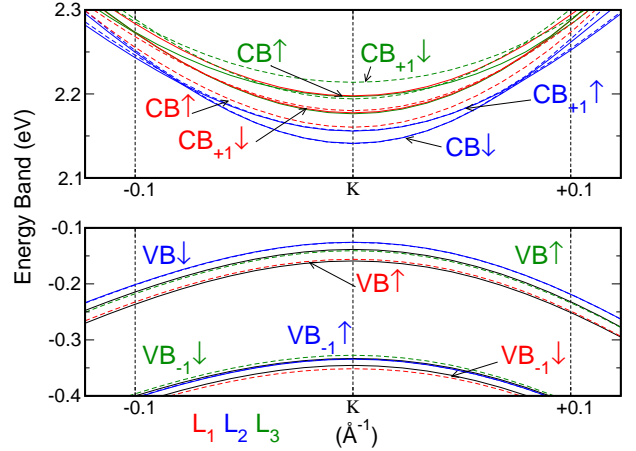


FIG. 12: **Valence and conduction bands shifts induced by an electric field.**  $G_0W_0$  band structure of 2H MoS<sub>2</sub> trilayer in the vicinity of K-point, without (solid lines) and with an applied electric field  $F_z = 1$  MV/cm value (dashed lines).  $L_1$  bands are in red,  $L_2$  bands are blue and  $L_3$  band are depicted in green.

in this case, due to symmetry of the conduction band  $d_{z^2}$  nature [16, 55, 56]. Interestingly, for the B-peak, originating mainly from  $VB_{-1,\uparrow}^{L_1} \rightarrow CB_{+1,\uparrow}^{L_1}$  and  $VB_{-1,\uparrow}^{L_2} \rightarrow CB_{+1,\uparrow}^{L_2}$  transitions, the interlayer contributions ( $VB_{\uparrow}^{L_2} \rightarrow CB_{+1,\uparrow}^{L_1}$  and  $VB_{\downarrow}^{L_1} \rightarrow CB_{+1,\downarrow}^{L_2}$ ) are already large for zero electric field and increase with enhanced electric field values. This means that the delocalization of the hole, even in the B-excitons, becomes more pronounced with electric field.

Exciton	A	IE <sub>1</sub>	IE <sub>2</sub>	B
	VB <sub>↓</sub> <sup>L<sub>1</sub></sup> → CB <sub>↓</sub> <sup>L<sub>1</sub></sup>	VB <sub>↓</sub> <sup>L<sub>1</sub></sup> → CB <sub>+1,↓</sub> <sup>L<sub>2</sub></sup>	VB <sub>↑</sub> <sup>L<sub>2</sub></sup> → CB <sub>+1,↑</sub> <sup>L<sub>1</sub></sup>	VB <sub>-1,↑</sub> <sup>L<sub>1</sub></sup> → CB <sub>+1,↑</sub> <sup>L<sub>1</sub></sup>
0.0 (MV/cm)	5%	13%	13%	17%
	VB <sub>-1,↓</sub> <sup>L<sub>2</sub></sup> → CB <sub>↓</sub> <sup>L<sub>1</sub></sup>	VB <sub>-1,↓</sub> <sup>L<sub>2</sub></sup> → CB <sub>+1,↓</sub> <sup>L<sub>2</sub></sup>	VB <sub>-1,↑</sub> <sup>L<sub>1</sub></sup> → CB <sub>+1,↑</sub> <sup>L<sub>1</sub></sup>	VB <sub>↑</sub> <sup>L<sub>2</sub></sup> → CB <sub>+1,↑</sub> <sup>L<sub>1</sub></sup>
0.5 (MV/cm)	6%	12%	14%	18%
1.0 (MV/cm)	5%	11%	15%	19%
2.0 (MV/cm)	5%	10%	18%	23%

TABLE I: **Decomposition of the oscillator strengths for 2H MoS<sub>2</sub> bilayer at the K point.** Identification of the main electron-hole pairs related to the excitonic peaks are indicated in the first line. The percentage of the second most important contribution to the oscillator strength is given for four different electric field values, its physical nature is indicated in the second line for  $F_z = 0$ . CB and VB denote conduction band and valence band. L<sub>1</sub> and L<sub>2</sub> indicate transitions in layer 1 and 2, respectively.

In contrast, the intralayer contribution to IE<sub>1</sub> tends to decrease with increasing electric field, while it increases for IE<sub>2</sub>, explaining the anticrossing regime observed between IE<sub>2</sub> and B lines.

#### 4. Trilayer case

In Table II, the percentages of the second main electron-hole pair contribution to the first excitonic peaks are given for the trilayer case in the absence of an electric field. A-peaks are related to two different transitions, namely A:1s L<sub>2</sub> and A:1s L<sub>1</sub>, L<sub>3</sub>, as can be observed from magneto-optics measurements, reported previously [12]. The contribution from the other layers to these oscillator strengths remains modest. The IE\* peak clearly results from interlayer transitions, in which the electron lies in L<sub>2</sub>, while the hole is delocalized over L<sub>1</sub> and L<sub>3</sub> (mediated by a small amount of intralayer L<sub>2</sub> coupling with good spin parity). For IE, the hole is almost exclusively in L<sub>2</sub>. It couples with an electron largely localized in L<sub>1</sub> and in lesser extent in L<sub>3</sub>. A first B-like exciton (B:1s L<sub>2</sub>), composed of the corresponding L<sub>2</sub> VB and CBs, appears in the spectrum with a small contribution from delocalized holes over L<sub>1,3</sub>. Additional B-like transitions (B:1s L<sub>1</sub>, L<sub>3</sub>), implying L<sub>1</sub> and L<sub>3</sub> VBs and CBs, also contribute to the spectrum.

A:1s L <sub>2</sub>	A:1s L <sub>1</sub> , L <sub>3</sub>	IE*	IE	B:1s L <sub>2</sub>	B:1s L <sub>1</sub> , L <sub>3</sub>
$\text{VB}_{\downarrow}^{\text{L}_2} \rightarrow \text{CB}_{\downarrow}^{\text{L}_2}$	$\text{VB}_{\uparrow}^{\text{L}_{1,3}} \rightarrow \text{CB}_{\uparrow}^{\text{L}_{1,3}}$	$\text{VB}_{\uparrow}^{\text{L}_{1,3}} \rightarrow \text{CB}_{+1,\uparrow}^{\text{L}_2}$	$\text{VB}_{\downarrow}^{\text{L}_2} \rightarrow \text{CB}_{+1,\downarrow}^{\text{L}_1}$	$\text{VB}_{-1,\uparrow}^{\text{L}_2} \rightarrow \text{CB}_{+1,\uparrow}^{\text{L}_2}$	$\text{VB}_{-1,\downarrow}^{\text{L}_{1,3}} \rightarrow \text{CB}_{+1,\downarrow}^{\text{L}_3}$
6%	4%	10%	18%	13%	40%
$\text{VB}_{-1,\downarrow}^{\text{L}_3} \rightarrow \text{CB}_{\downarrow}^{\text{L}_2}$	$\text{VB}_{-1,\uparrow}^{\text{L}_2} \rightarrow \text{CB}_{\uparrow}^{\text{L}_{1,3}}$	$\text{VB}_{-1,\uparrow}^{\text{L}_2} \rightarrow \text{CB}_{+1,\uparrow}^{\text{L}_2}$	$\text{VB}_{\downarrow}^{\text{L}_2} \rightarrow \text{CB}_{+1,\downarrow}^{\text{L}_3}$	$\text{VB}_{\uparrow}^{\text{L}_1} \rightarrow \text{CB}_{+1,\uparrow}^{\text{L}_2}$	$\text{VB}_{-1,\downarrow}^{\text{L}_{3,1}} \rightarrow \text{CB}_{+1,\downarrow}^{\text{L}_3}$

TABLE II: **Decomposition of the oscillator strengths for 2H MoS<sub>2</sub> trilayer at the K point without electric field.** Identification of the two main electron-hole pairs related to excitonic peaks and percentage of the second contribution to the total oscillator strength.

- [1] Chernikov, A. *et al.* Exciton binding energy and nonhydrogenic Rydberg series in monolayer WS<sub>2</sub>. *Phys. Rev. Lett.* **113**, 076802 (2014).
- [2] Wang, G. *et al.* Colloquium: Excitons in atomically thin transition metal dichalcogenides. *Rev. Mod. Phys.* **90**, 021001 (2018).
- [3] Scuri, G. *et al.* Large excitonic reflectivity of monolayer MoSe<sub>2</sub> encapsulated in hexagonal boron nitride. *Phys. Rev. Lett.* **120**, 037402 (2018).
- [4] Back, P., Zeytinoglu, S., Ijaz, A., Kroner, M. & Imamoglu, A. Realization of an electrically tunable narrow-bandwidth atomically thin mirror using monolayer MoSe<sub>2</sub>. *Phys. Rev. Lett.* **120**, 037401 (2018).
- [5] Rivera, P. *et al.* Observation of long-lived interlayer excitons in monolayer MoSe<sub>2</sub>-WSe<sub>2</sub> heterostructures. *Nature Communications* **6**, 6242 (2015).
- [6] Joe, A. Y. *et al.* Electrically controlled emission from triplet charged excitons in atomically thin heterostructures (2019). arXiv1912.07678.
- [7] Unuchek, D. *et al.* Valley-polarized exciton currents in a van der Waals heterostructure. *Nature Nanotechnology* **14**, 1104–1109 (2019).
- [8] Nagler, P. *et al.* Interlayer exciton dynamics in a dichalcogenide monolayer heterostructure. *2D Materials* **4**, 025112 (2017).
- [9] Förg, M. *et al.* Cavity-control of interlayer excitons in van der Waals heterostructures. *Nature Communications* **10**, 3697 (2019).
- [10] Slobodeniuk, A. *et al.* Fine structure of K-excitons in multilayers of transition metal dichalcogenides. *2D Materials* **6**, 025026 (2019).
- [11] Calman, E. *et al.* Indirect excitons in van der Waals heterostructures at room temperature. *Nature Communications* **9**, 1895 (2018).
- [12] Gerber, I. C. *et al.* Interlayer excitons in bilayer MoS<sub>2</sub> with strong oscillator strength up to room temperature. *Physical Review B* **99**, 035443 (2019).
- [13] Niehues, I., Blob, A., Stiehm, T., de Vasconcellos, S. M. & Bratschitsch, R. Interlayer excitons in bilayer MoS<sub>2</sub> under uniaxial tensile strain. *Nanoscale* **11**, 12788–12792 (2019).
- [14] Carrasco, F., Lin, D.-Y., Frisenda, R. & Castellanos-Gomez, A. Biaxial strain tuning of interlayer excitons in bilayer MoS<sub>2</sub>. *Journal of Physics: Materials* **3**, 015003 (2019).
- [15] Pisoni, R. *et al.* Absence of interlayer tunnel coupling of K-valley electrons in bilayer MoS<sub>2</sub>. *Phys. Rev. Lett.* **123**, 117702 (2019).
- [16] Gong, Z. *et al.* Magnetoelectric effects and valley-controlled spin quantum gates in transition metal dichalcogenide bilayers. *Nature Communications* **4**, 2053 (2013).
- [17] Roch, J. G. *et al.* Quantum-confined Stark effect in a MoS<sub>2</sub> monolayer van der Waals heterostructure. *Nano Letters* **18**, 1070–1074 (2018).
- [18] Verzhbitskiy, I., Vella, D., Watanabe, K., Taniguchi, T. & Eda, G. Suppressed out-of-plane polarizability of free excitons in monolayer wse<sub>2</sub>. *ACS Nano* **13**, 3218–3224 (2019).
- [19] Arora, A. *et al.* Interlayer excitons in a bulk van der Waals semiconductor. *Nature Communications* **8**, 639 (2017).
- [20] Cristofolini, P. *et al.* Coupling quantum tunneling with cavity photons. *Science* **336**, 704–707 (2012).
- [21] Schneider, C., Glazov, M. M., Korn, T., Höfling, S. & Urbaszek, B. Two-dimensional semiconductors in the regime of strong light-matter coupling. *Nature Communications* **3**, 2695 (2018).
- [22] Muñoz-Matutano, G. *et al.* Emergence of quantum correlations from interacting fibre-cavity polaritons. *Nature Materials* **18**, 213 (2019).
- [23] Delteil, A. *et al.* Towards polariton blockade of confined exciton-polaritons. *Nature Materials* **18**, 219 (2019).
- [24] Miller, D. A. *et al.* Band-edge electroabsorption in quantum well structures: The quantum-confined Stark effect. *Physical Review Letters* **53**, 2173 (1984).
- [25] Roch, J. G. *et al.* Spin-polarized electrons in monolayer MoS<sub>2</sub>. *Nature Nanotechnology* **14**, 432–436 (2019).
- [26] Nagler, P. *et al.* Interlayer excitons in transition-metal dichalcogenide heterobilayers. *physica status solidi (b)* **256**, 1900308 (2019).
- [27] Wu, S. *et al.* Electrical tuning of valley magnetic moment through symmetry control in bilayer MoS<sub>2</sub>. *Nature Physics* **9**, 149 (2013).
- [28] Jones, A. M. *et al.* Spin-layer locking effects in optical orientation of exciton spin in bilayer WSe<sub>2</sub>. *Nature Physics* **10**, 130–134 (2014).
- [29] Lindlau, J. *et al.* The role of momentum-dark excitons in the elementary optical response of bilayer WSe<sub>2</sub>. *Nature Communications* **9**, 2586 (2018).
- [30] Wang, Z., Chiu, Y.-H., Honz, K., Mak, K. F. & Shan, J. Electrical tuning of interlayer exciton gases in WSe<sub>2</sub> bilayers. *Nano Letters* **18**, 137–143 (2017).
- [31] Horng, J. *et al.* Observation of interlayer excitons in MoSe<sub>2</sub> single crystals. *Phys. Rev. B* **97**, 241404 (2018).
- [32] Shimazaki, Y. *et al.* Moiré superlattice in a MoSe<sub>2</sub>/hBN/MoSe<sub>2</sub> heterostructure: from coherent coupling of inter- and intra-layer excitons to correlated mott-like states of electrons (2019). arXiv1910.13322.
- [33] Sung, J. *et al.* Broken mirror symmetry in excitonic response of reconstructed domains in twisted MoSe<sub>2</sub>/MoSe<sub>2</sub> bilayers (2020). arXiv2001.01157.
- [34] Deilmann, T. & Thygesen, K. S. Interlayer excitons with large optical amplitudes in layered van der Waals materials. *Nano Letters* **18**, 2984–2989 (2018).
- [35] Taniguchi, T. & Watanabe, K. Synthesis of high-purity boron nitride single crystals under high pressure by using ba-bn solvent. *Journal of Crystal Growth* **303**, 525 – 529 (2007).
- [36] Novoselov, K. S. *et al.* Two-dimensional atomic crystals. *Proceedings of the National Academy of Sciences* **102**, 10451–10453 (2005).
- [37] Back, P. *et al.* Giant paramagnetism-induced valley polarization of electrons in charge-tunable monolayer MoSe<sub>2</sub>. *Phys. Rev. Lett.* **118**, 237404 (2017).
- [38] Robert, C. *et al.* Optical spectroscopy of excited exciton states in mos<sub>2</sub> monolayers in van der Waals heterostructures. *Phys. Rev. Materials* **2**, 011001 (2018).
- [39] Laturia, A., Van de Put, M. L. & Vandenberghe, W. G. Dielectric properties of hexagonal boron nitride and transition metal dichalcogenides: from monolayer to bulk. *npj 2D Materials and Applications* **2**, 6 (2018).

- [40] Kresse, G. & Hafner, J. *Ab initio* molecular dynamics for liquid metals. *Phys. Rev. B* **47**, 558–561 (1993).
- [41] Kresse, G. & Furthmüller, J. Efficient iterative schemes for *ab initio* total-energy calculations using a plane-wave basis set. *Phys. Rev. B* **54**, 11169–11186 (1996).
- [42] Blöchl, P. E. Projector augmented-wave method. *Phys. Rev. B* **50**, 17953 (1994).
- [43] Kresse, G. & Joubert, D. From ultrasoft pseudopotentials to the projector augmented-wave method. *Phys. Rev. B* **59**, 1758–1775 (1999).
- [44] Grimme, S., Antony, J., Ehrlich, S. & Krieg, H. A consistent and accurate *ab initio* parametrization of density functional dispersion correction (DFT-D) for the 94 elements H-Pu. *J. Chem. Phys.* **132**, 154104–19 (2010).
- [45] Heyd, J. & Scuseria, G. E. Assessment and validation of a screened Coulomb hybrid density functional. *J. Chem. Phys.* **120**, 7274 (2004).
- [46] Heyd, J., Peralta, J. E., Scuseria, G. E. & Martin, R. L. Energy band gaps and lattice parameters evaluated with the Heyd-Scuseria-Ernzerhof screened hybrid functional. *J. Chem. Phys.* **123**, 174101 (2005).
- [47] Paier, J. *et al.* Screened hybrid density functionals applied to solids. *J. Chem. Phys.* **124**, 154709 (2006).
- [48] Shishkin, M. & Kresse, G. Implementation and performance of the frequency-dependent *gw* method within the *paw* framework. *Phys. Rev. B* **74**, 035101 (2006).
- [49] Mostofi, A. A. *et al.* wannier90: A tool for obtaining maximally-localised Wannier functions. *Computer Physics Communications* **178**, 685–699 (2008).
- [50] Hanke, W. & Sham, L. J. Many-Particle Effects in the optical Excitations of a semiconductor. *Phys. Rev. Lett.* **43**, 387 (1979).
- [51] Rohlfing, M. & Louie, S. G. Electron-hole Excitations in Semiconductors and Insulators. *Phys. Rev. Lett.* **81**, 2312–2315 (1998).
- [52] Ramasubramaniam, A., Naveh, D. & Towe, E. Tunable band gaps in bilayer transition-metal dichalcogenides. *Physical Review B* **84**, 205325–10 (2011).
- [53] Xiao, J. *et al.* Effects of van der Waals interaction and electric field on the electronic structure of bilayer MoS<sub>2</sub>. *Journal of Physics: Condensed Matter* **26**, 405302 (2014).
- [54] Lu, X. & Yang, L. Stark effect of doped two-dimensional transition metal dichalcogenides. *Applied Physics Letters* **111**, 193104–6 (2017).
- [55] Akashi, R. *et al.* Two-Dimensional Valley Electrons and Excitons in Noncentrosymmetric 3R-MoS<sub>2</sub>. *Physical Review Applied* **4**, 1467–7 (2015).
- [56] Kormanyos, A. *et al.* *k.p* theory for two-dimensional transition metal dichalcogenide semiconductors. *2D Materials* **2**, 022001 (2015).

**Acknowledgements.**— (\*) N.L. S.S, I.P. and L.S. contributed equally to this work. Basel acknowledges funding from the PhD School *Quantum Computing and Quantum Technology*, SNF (Project No.200020\_156637) SwissNanoscience Institute (SNI) and NCCR QSIT. Toulouse acknowledges funding from ANR 2D-vdW-Spin, ANR VallEx, ANR MagicValley, ITN 4PHOTON Marie Skłodowska Curie Grant Agreement No. 721394 and the Institut Universitaire de France. K.W. and T.T. acknowledge support from the Elemental Strategy Initiative conducted by the MEXT, Japan and the CREST(JPMJCR15F3), JST. I.C.G. thanks the CALMIP initiative for the generous allocation of computational times, through the project p0812, as well as the GENCI-CINES and GENCI-IDRIS for the grant A006096649. We thank Jean-Marie Pumirol for AFM measurements.